Nondestructive evaluation of fused filament fabrication 3D printed structures using optical coherence tomography

Lucas Ramos De Pretto
Center for Lasers and Applications, Nuclear and Energy Research Institute, IPEN–CNEN/SP, São Paulo, Brazil
Marcello Magri Amaral
Universidade Brasil, São Paulo, Brazil, and
Anderson Zanardi de Freitas and Marcus Paulo Raele
Center for Lasers and Applications, Nuclear and Energy Research Institute, IPEN–CNEN/SP, São Paulo, Brazil

Abstract

Purpose – The quality of components under fused filament fabrication (FFF) is related to the correct filament spacing and bonding of successively deposited layers and is evaluated mainly by scanning electron microscopy (SEM). However, it is a destructive technique and real-time evaluation is not possible. Optical coherence tomography (OCT), on the other hand, is an optical method that acquires cross-sectional images non-invasively and in real-time. Therefore, this paper aims to propose and validate the use of OCT as a non-destructive quality evaluation tool for FFF using Polylactic Acid (PLA) filaments.

Design/methodology/approach – PLA three-dimensional (3D) printed samples were made in a variety of nozzle temperatures and mesh spacing. These samples were fractured in liquid nitrogen and inspected using SEM (as a gold standard) to evaluate dimensions and morphology, then the samples were evaluated by OCT in the same area, allowing the results confrontation.

Findings – Our results indicate a good correlation between OCT and SEM for the dimensional assessment of layers. When the filament was extruded in lower temperatures, the OCT images presented sharply defined interfaces between layers, in contrary to higher nozzle temperatures, denoting better fusion between them. However, higher extruding temperatures are incurred in greater deviations from nominal dimensions of the mesh. Finally, we demonstrate the advantage of a full 3D tomographic reconstruction to inspect within a FFF sample, which enabled the inspection of "hidden" information, not visible on a single cross-sectional cut.

Originality/value – This paper proposes OCT as a novel and nondestructive evaluation tool for FFF.

Keywords Fused filament fabrication, Fused deposition modeling, 3D printing, OCT, Optical coherence tomography, Adhesion, 3D printing evaluation

Paper type Research paper

Introduction

Additive manufacturing (AM), sometimes referred to as three-dimensional (3D) printing, is a thriving technique that is one of the catalyzers of the new industrial revolution (Berman, 2012), allowing the production of parts to virtually all areas of knowledge, from the automotive industry to medicine (Rengier *et al.*, 2010; Guo and Leu, 2013), opening the possibility of customization, real-time and *in situ* production.

Increasing demand for AM, following the current worldwide trend toward digital industrial technologies, has led to the development of diverse 3D-printing techniques. Among those, fused filament fabrication (FFF) – also known as fused deposition modeling (FDM) – is gaining popularity among hobbyists, designers and small businesses, as it enables the production of plastic (polymeric) models with low investment (Song *et al.*, 2017). Furthermore, open-source equipment, free software and the uncountable models made freely available by cooperative databases are catalysts for FFF adoption.

The principle for FFF is based on an extruder that pushes melted polymer through a heated nozzle. The nozzle moves on a predetermined path, depositing a thin trail of plastic (called "road"). Once one path is finished, the sample (or the nozzle) is displaced in the axial direction and the deposition of roads resumes on a new path. The organized superposition of roads forms the layers of the 3D model being manufactured.

A key factor for 3D-printed objects is its mechanical strength (Tymrak *et al.*, 2014), a property that defines the range of applications for a given model. Because of the printing process,

The current issue and full text archive of this journal is available on Emerald Insight at: **https://www.emerald.com/insight/1355-2546.htm**

Rapid Prototyping Journal
26/10 (2020) 1853–1860
 [ISSN 1355-2546]
[DOI 10.1108/RPJ-12-2019-0314]

The authors thank the support of the São Paulo Research Foundation (FAPESP) through the processes #2015/15775–3, #2017/21851–0, #2018/20226–7 and #2019/19465–0; the National Council for Scientific and Technological Development (CNPq) grants #449440/2014–1, #422484/2016–4. The authors also acknowledge the support given by the Center for Lasers and Applications' Multi-user Facility at IPEN-CNEN/SP.

Received 11 December 2019
Revised 29 July 2020
27 August 2020
Accepted 21 September 2020

FFF usually has two different structural patterns (anisotropy): one along the direction of the roads (X and Y) and the other following the layers' growth direction (Z). For X and Y the mechanical strength properties are related to the extruded roads, while for Z the strength is closely related to the adhesion between layers (Torrado Perez *et al.*, 2014; McIlroy and Olmsted, 2017; Song *et al.*, 2017).

Several approaches have been proposed to visually evaluate the quality of FFF printed samples, analyzing factors such as dimensional accuracy, layer bonding and mechanical strength among many others, which relate to the fabricated part applicability to its intended use. One such study is by Costa, using Microtome to analyze layer bonding and dimensional accuracy across different printing configurations (Costa *et al.*, 2019). Davis *et al* has also used Microtome together with Optical Microscopy to evaluate the correlation between contact area size and adhesion between layers (Davis *et al.*, 2017). Lanzotti *et al* used scanning electron microscopy (SEM) to study the effect of different printing parameters on nominal strain at break (Lanzotti *et al.*, 2015). Similarly, Kuznetsov applied SEM to analyze how different printing parameters affect the breaking force (Kuznetsov *et al.*, 2018). Varying printing conditions were also studied through Optical Microscopy by Gebisa and Lemu, relating them to the flexural properties of the samples (Gebisa and Lemu, 2018). Finally, Hollister *et al* have used a 3D evaluation technique, Micro-CT, but did not aim to inspect the printing quality itself, but the bone formation surrounding the 3D printed structure (Hollister *et al.*, 2015). More thorough reviews of FFF evaluation are available in the literature, for the interested reader (Kim *et al.*, 2018; Cuan-Urquizo *et al.*, 2019).

Some characteristics, such as mechanical strength or flexural strength may be evaluated directly, though destructive processes and specialized equipment. Nonetheless, as the aforementioned studies indicate, some of these features can also be estimated by visual inspection of the samples, which greatly reduces the complexity of testing. To this end, one may note that techniques such as Optical Microscopy (Davis *et al.*, 2017; Gebisa and Lemu, 2018) and SEM (Lanzotti *et al.*, 2015; Kuznetsov *et al.*, 2018; Wu *et al.*, 2018), are commonly applied. However, those tests require preprocessing of the samples (oftentimes destructive) to obtain a cross-sectional view of the extruded roads and, for some samples, even conductive coatings are necessary for imaging to be performed. Of the images techniques mentioned, only Micro-CT can perform an inspection of internal structures non-destructively but is an expensive option.

Optical coherence tomography (OCT) (Huang *et al.*, 1991; De Freitas *et al.*, 2010) is an optical interferometric technique based on light backscattered from a sample, providing cross-sectional tomographic images with a resolution on the order of a few micrometers. OCT uses a beam from a broadband light source which is split, by a beam splitter (BS), into two optical paths, usually based on a Michelson Interferometer, as illustrated in Figure 1. The two waves are later reflected and/or backscattered, recombined and detected, producing an interferometric signal.

OCT is non-destructive, non-contact, applicable to any scattering media (such as polylactic acid – PLA) and does not require any preprocessing of the sample. Recent studies in the AM literature have explored the applicability of OCT on

Figure 1 OCT principle of operation

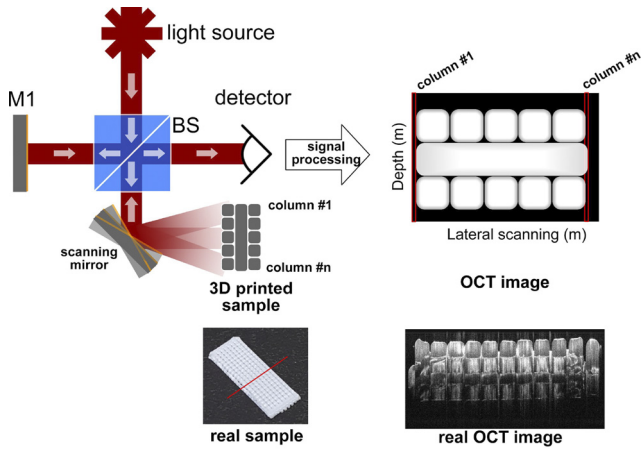

Notes: A beam of light with a broadband emission, represented by G(k), is directed to a beam splitter (BS), directing part of the radiation to a reference mirror (M1); the other part is directed to the sample, in which backscattering occurs not only at the surface but also inside the sample. The samples' backscattered light goes back to the BS, where it is recombined with the reference light beam reflected by M1, giving rise to an interferometric pattern which, after processing, results in a single column of the final OCT image, containing information on the backscattering locations. Scanning the light beam across the sample and collecting successive columns, allow the system to form a full OCT image

selective laser sintering (SLS) and selective laser melting (SLM) applications, assessing surface roughness (DePond *et al.*, 2018) and defects (Hirsch *et al.*, 2017), as well as subsurface characteristics (Guan *et al.*, 2015; Gardner *et al.*, 2018). However, investigations on the use of OCT as a nondestructive evaluation (NDE) method for other materials, such as PLA (which is, at the time of writing, one of the most used materials for FFF), are still lacking. To the best of our knowledge, the use of the OCT system for this purpose has not been reported.

Therefore, the aim of this study is to fill this gap in the literature, demonstrating the use of OCT as a tool for assessment of FFF manufacturing quality, exploring its inherent advantages as a tomographic NDE technique and evaluating its limitations when compared to the widely used SEM approach.

Dimensional and morphological features are among the most valuable information on the production quality of FFF parts, supporting the rationale and goal of the present work: evaluate the potential of OCT as a non-destructive dimensional and morphological evaluation tool for inspecting FFF structures printed using PLA.

Materials and methods

Fused filament fabrication sample preparation

In this work, we used a FFF 3D printer (CL1 Black edition – Cliever, Brazil) loaded with PLA filament (brand 3DFila, pearl white color and 1.75 mm diameter) to build the 3D printed

samples. This printer allows printing components with nominal road thickness ranging from 100 to 250 μm.

Figure 2a presents the computational 3D model designed in SolidWorks® (Dassault Systems). For this base model, the height of each layer (h) was set as 200 μm, the thickness of each road (t) was defined as 500 μm, the total length of the sample was 1,500 μm and the total width varied between 4.8 mm and 5.6 mm, depending on the spacing(s) configuration.

The 3D model was uploaded to the printer proprietary software to print the sample (Figure 2b).

For this study, we have printed five samples with a constant temperature while varying "s" and three samples with a constant "s" while varying the temperature. On each of those samples, five roads were analyzed. One additional sample, with a different middle layer, was printed for 3D evaluation with OCT.

Scanning electron microscopy system

The SEM images were acquired by using a HITACHI TM3000 SEM equipment (tabletop). The samples were immersed in liquid nitrogen and then fractured transversally, as indicated in Figure 2a. Images of the fractured facet were acquired on the SEM system with a magnification of 30x and 5 kV potential difference.

Optical coherence tomography system

We used a commercial spectral OCT system (OCP930SR – Thorlabs Inc.) working at 930 nm (100 nm FWHM), providing an axial resolution of 6 μm in air. For each sample, three different cross-sectional images of 1024 × 512 pixels, covering 6 mm × 1.6 mm (lateral and axial, respectively) were acquired along the fracture line (Figure 2a). As our system does not have longitudinal beam scanning, to enable a full 3D sampling a motorized translation stage was used to displace the sample while images were continuously acquired.

Statistical analysis

All acquired data was tested regarding normality using the Kolmogorov-Smirnov test. For the comparison between OCT and SEM acquired measurements it was performed the t-test, for parametric data or Mann-Whitney test, for non-parametric data, with a significance level of $p = 0.05$ using Minitab Statistical Software 18 (Minitab Inc., State College, PA).

Figure 2 Drawing of the sample used. Road width is denoted by "w," road height by "h," road spacing by "s"

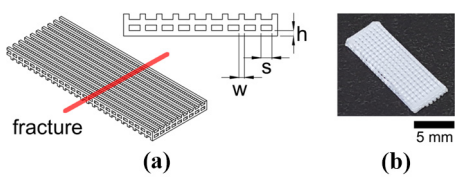

Notes: The samples were fractured transversely, as denoted by the thick red line. On the right side, the photography of a representative sample

Experiments and analysis

Refractive index correction

As OCT is an optical-based technique, the images produced are distorted by the refractive index (n) of the material under study, as it alters the optical path of the beam going back and forth inside the sample. The dimensional evaluation, therefore, must take into account the aberrations induced, which requires knowledge of n.

Conveniently, OCT itself may be used to determine the refractive index of some samples, as is the case of PLA. To do so, one needs to compare the measured optical length (or thickness) of the sample of interest with an unknown refractive index, with a measurement where the refractive index of the medium is well defined (such as air, $n \rightarrow 1$), as shown in Figure 3, with a PLA sample.

Note that the flat glass surface, on which the sample was placed, appears distorted (shifted) under the sample, generating an image artifact (a discontinuity on its depth position) due to the physical phenomenon related – the optical path through the sample is longer than through the air. The ratio between optical thickness (ot) and physical thickness (pt) of the sample yields its refractive index. To carry out such an experiment with OCT all that is required is that the beam traverses the whole sample and probes a reference structure underneath it (e.g. the glass surface). Worth mentioning, however, is that the refractive index is wavelength dependent.

In our study, three PLA samples (single 200 μm layer) were printed for refractive index measurements. Five sets of measurements were carried out for each one, and the effective refractive index was considered to be the average value of those 15 repeats. The resulting refractive index of PLA for the wavelengths of our OCT system was 1.48 ± 0.04 (mean $\pm$ standard deviation). This value is in good agreement with the literature (Goncalves *et al.*, 2010). Once the refractive index is known, all depth (z-axis) related measurements can be corrected by a simple division by n. The authors have performed this adjustment on all applicable measurements.

Even though the refractive index for a myriad of materials may be readily found in the literature, the authors recommend

Figure 3 Refractive index measurement process using OCT

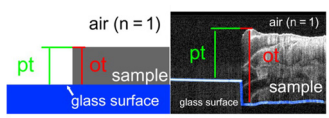

Notes: On the left: the schematic illustration of the process, which consists of measuring the sample from the outside (refractive index equal to 1) where it will provide the pt, and probing the sample through its medium (PLA), which will provide its o). On the right: the OCT image, where the distortion due to the refractive index is clearly visible, as the flat glass surface appears to have a discontinuity under the sample. The pt/ot ratio, then, provides the PLA refractive index

the described experiment to be carried out for studies using OCT as an NDE tool for AM, whenever applicable. This is due to the fact that, for some samples, the material composition and, thus, the refractive index, may vary slightly between manufacturers (as in the case of PLA filaments from different brands) and, additionally, OCT uses a broadband light source, and the optical path deformations are a result of the material's refractive index across different wavelengths. The result from the described procedure is an effective refractive index directly calculated for the OCT system and sample used and intrinsically accounts for both aspects highlighted.

Dimensional assessment using optical coherence tomography

For this experiment, the printing mesh separation "*s*" (Figure 2) was varied in the 3D virtual model, and one sample was printed for each separation value (mesh). The nominal separations were: 0, 20, 50, 100, 150 and 200 μm. All samples were printed with the same nozzle temperature of 175°C (chosen based on the filament and 3D printer specifications). After printing the samples, they were immersed in liquid nitrogen and fractured as described previously.

Figure 4 presents the SEM and OCT images of those 3D printed samples with different mesh parameters. The correlation between SEM and OCT images is easily observed.

We performed dimensional measurements of different aspects of the printed samples: layer height, road width and separation ("h", "t' and "*s*", respectively, according to Figure 2) using the OCT system in a region near the fractured facet. The same measurements were performed on SEM inspecting the facet *en face*.

For each mesh value, five different PLA roads were selected and measured on both images. For the spacing measurements, the gap to the right of each selected road was evaluated. Figure 5 presents the mean value and standard deviation for each of the measured parameters. We highlight that, for the spacing of 0.02 mm, only three gaps were observed in the images, meaning that the spacing for the majority of the mesh was 0 mm. To observe agreement between OCT and SEM measurements, Bland-Altman plots comparing both techniques are also presented in Figure 6.

Across all measurements, it was observed a statistically relevant agreement between OCT and SEM ($p > 0.37$; worst p-value for all the comparison) on all used mesh for the measured parameters in PLA. The Bland-Altman plots also reinforce that measurements made with both techniques are in close agreement, as almost all of the data points fall within the agreement region (95% confidence interval).

The height and width measurements are closely correlated. While the height increases after a mesh separation of 50 μm, the width values drop, decreasing the aspect ratio (width/height) of each road. This behavior is due to heated PLA spreading laterally after deposition. Nevertheless, as all mesh patterns were printed with the same nozzle temperature, we hypothesize that the higher aspect ratio values for denser structures are due to hot material being deposited (printed) heating up adjacent roads (already printed), allowing them to spread out further. When the spacing is increased past a certain distance, the heat transfer is minimized and this effect is no longer observed. This observation is in accordance with other FFF studies that demonstrate that the gap between deposited layers affect the heat transfer and/or loss of the material, which, in turn, has an influence on the spread of the semi-molten plastic and the mechanical properties of the sample (Mohamed *et al.*, 2016; Gebisa and Lemu, 2018). This reasoning also explains why the roads are larger for the case of 20 μm spacing – the gaps in the mesh are filled out as the roads spread, resulting in only three visible openings in our analysis. With 0 mm spacing, there is less room for the adjacent roads to expand laterally, and from 50 μm onwards the heating is not enough to promote appreciable deformations. The aspect ratio remains reasonably stable from 50 μm-200 μm spacings. This aspect ratio behavior can be visualized on the full SEM and OCT images present in Figure 4a – the smaller spacings present widened roads, while the larger ones are narrower and similar.

Considering the only the spacings of 50 μm or larger, the average road width (t) was 438 μm ± 5 μm for OCT and 435 μm ± 3 μm for SEM. The values are in statistical agreement ($p > 0.05$), however, are distant from the nominal 500 μm. On the same set of samples, the average height (h) was 195 μm ± 1 μm for OCT and 196 μm ± 2 μm for the reference value, once again in statistical accordance ($p > 0.05$) – given the system resolution – and, this time, not far from the intended 200 μm. This reveals that the calibration for the FFF printer

Figure 4 Comparison of SEM and OCT images of the 3D printed samples for each used mesh separation parameter(s)

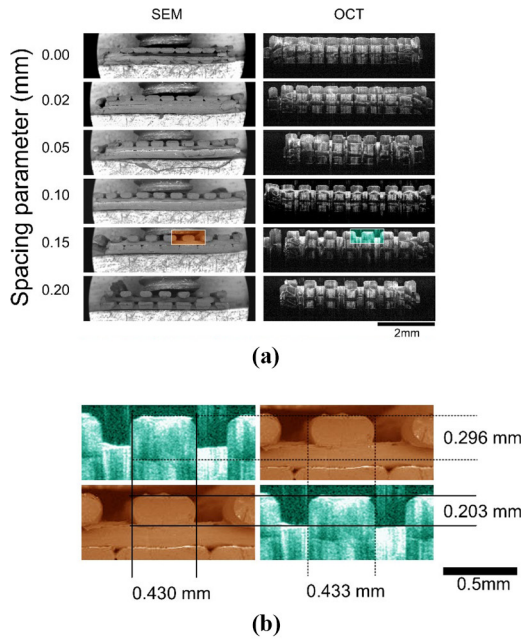

Notes: (a) Full image comparison for the printed samples, with SEM images on the left and OCT images on the right, (b) Expanded view of the highlighted areas for the 0.15 mm spacing on (a). Note that the height measured with OCT (0.296 mm) after correction by the refractive index (0.200 mm) is in good agreement with the SEM measurement (0.203 mm). Additionally, the bottom row on (b) shows how the physical thickness (pt), as measured by SEM, is also in good agreement with OCT when probed through the air (where $n = 1$)

used in this experiment was not optimal, and a technique such as OCT may be used as a feedback source to that end.

The obtained spacings values increased as the mesh got sparser, but do not present the expected linear trend. The results indicate that the printer slightly overshot each of the intended spacings, with the worst outcome occurring at the mesh of 100 μm (0.1 mm), which produced gaps of 161 μm $\pm$ 10 μm according to OCT data and 166 μm $\pm$ 10 μm calculated with SEM. Once again, a calibration feedback loop could be implemented with OCT integrated into the fabrication process. Apart from the 0 mm spacing sample, only the largest mesh of 200 μm had good results, with actual gaps measuring 223 μm $\pm$ 12 μm in OCT analysis and 212 μm $\pm$ 22 μm in our gold standard SEM. This type of visual inspection may prove crucial for sample quality assessment, as the gaps between roads (and even the height of the threads) are detrimental to the overall interlayer cohesion (Kuznetsov *et al.*, 2018). Therefore, sample deviations from its nominal specifications, be it because of printer limitations or thermal effects, may induce undesirable consequences to its mechanical properties.

Additionally, we highlight that on OCT images it is possible to identify all four layers of the printed samples. The bright spots inside the filaments on OCT images are associated with inhomogeneities on the material or to light polarization rotation, caused by material stress due to plastic smearing in the FFF process prior to cooling; alignment of polymers molecules may also result in birefringence, which could be investigated in detail using a polarization-sensitive OCT in future studies.

Figure 5 Dimensional assessment of different mesh structures

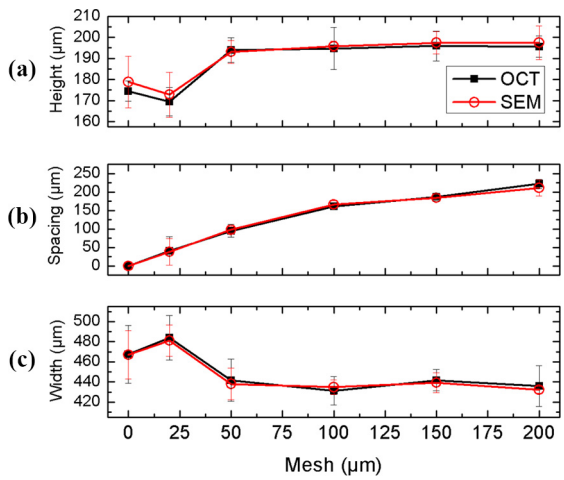

Notes: Measurements made with OCT are shown in black filled squares, while those made with SEM are shown in red outlined circles. It is possible to observe a good correlation between OCT and SEM on all measured aspects of the sample: (A) Height, (B) Spacing between filaments and (C) Width of printed roads. The unusual behavior observed for smaller spacings on (A) and (C) may be explained by the residual heating from filaments deposited adjacently

Temperature study

To further demonstrate the effect of heat on material deformation, we printed additional structures (as in Figure 2) using an "*s*" of 50 μm for all samples. This value for "*s*" was chosen based on the results for the dimensional assessment, to avoid heat transfer between adjacent deposited roads. However, the samples were printed using different nozzle temperatures: 155°C, 175°C and 195°C. The printed samples were also fractured transversely to the longest printing direction (as illustrated in Figure 2a), after immersion in liquid nitrogen.

Figure 7 presents the SEM and OCT images for each temperature condition, maintaining the mesh constant to 0.05 mm. With the increase of nozzle temperature, the filament stays longer at melting temperature, causing a distortion in the fused filament shape, similar to what we observed in the denser structures in the previous test set. Although there is no significant difference from the temperatures of 155°C and 175°C, the roads become flattered and wider for the 195°C sample. In OCT images, its observed width was 513 μm $\pm$ 24 μm, and in SEM it was 508 μm $\pm$ 20 μm ($p > 0.08$; worst p-value for all the comparison), much larger than the respective 448 μm $\pm$ 24 μm and 446 μm $\pm$ 18 μm for 175°C. Once more, assuming a constant volume of material being deposited, the height variation is expected to be inversely proportional to width variation, which was confirmed, with an average height reduction of, approximately, 33 μm according to OCT measurements and

Figure 6 Bland-Altman plots comparing the OCT and SEM 3D measurements for height, spacing and width of the 3D samples printed with different spacings

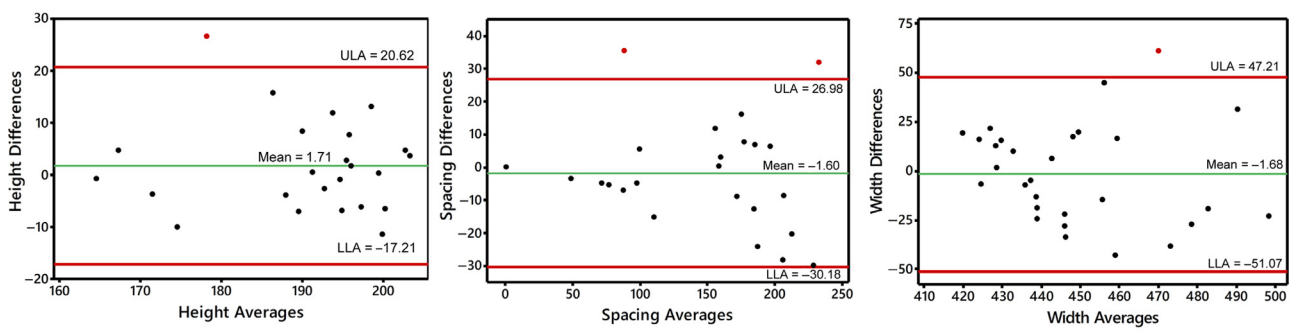

Notes: The green line represents the mean of the data points, while the red lines indicate the upper limit agreement (ULA) and lower limit agreement (LLA) for a 95% confidence interval. Both techniques have high agreement on all measured features

42 μm according to our gold standard. As a consequence of the filament distortion, the spacing between filaments is altered, resulting in no gap between roads for the 195°C sample. This behavior is observed in both, SEM and OCT. Those findings are shown in the graphs in Figure 8 and, along with Bland-Altman plots in Figure 9, one can observe, once more, the high agreement between SEM and OCT results.

Once again, the spread of the semi-molten material has a potential influence on the final properties of the sample, as it fills the voids between adjacent roads. While this reduction of gaps may induce better mechanical properties (Gebisa and Lemu, 2018; Kuznetsov *et al.*, 2018), it is still not the desired geometry for the sample and imparts a lower printed accuracy.

A further, related, qualitative observation is possible using OCT images. At 155°C (nozzle temperature) it is possible to observe higher reflectivity between different layers filaments (brighter region pointed by arrow *a* in Figure 7). The presence of that high reflectivity region is reduced as the temperature increases, and the layer border definition becomes less obvious (arrows *b* and *c* in Figure 7). The higher reflectivity is visible due to a discontinuity (gap) on the polymer fusion between the deposited layers – a change in the refractive index as the light goes from the PLA to air and, then, back to PLA, causing an OCT signal spike. On the other hand, when the nozzle is hotter the fusion of the layers is better (the gaps are filled by the semi-

Figure 7 Top: Full OCT (on the right) and SEM (left) images for each temperature condition

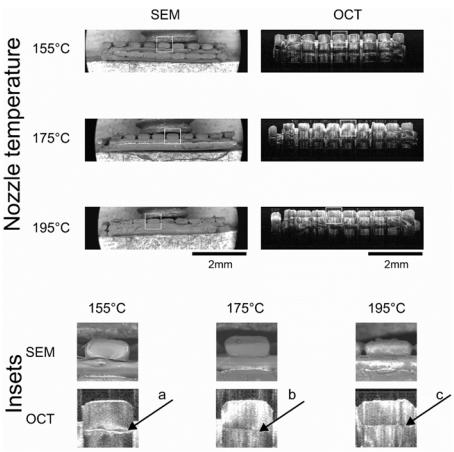

Notes: The mesh separation (s) was maintained constant to 50 µm. Bottom: Insets taken from the colored boxes on the full images, highlighting the visualization of interfaces between successive layers, indicated by the a, b and c labeled arrows

Figure 8 Dimensional assessment of samples printed with different nozzle temperatures

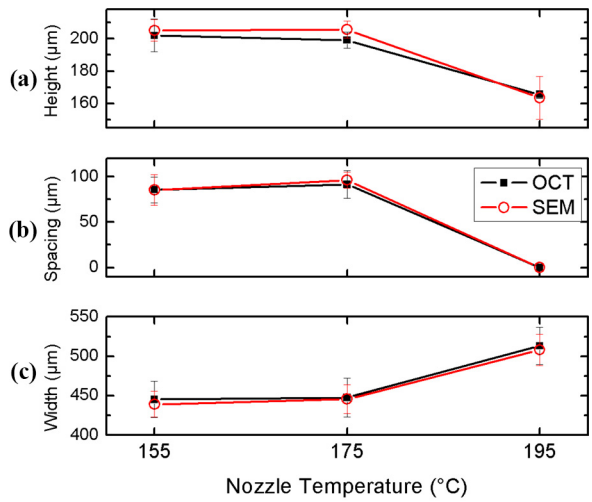

Notes: As before, measurements made with OCT are shown in black filled squares, and those made with SEM are displayed as red outlined circles. The aspects of interest are (A) Height, (B) Spacing between filaments and (C) Width of each road. Once again, results from OCT images are in good agreement (within one standard deviation) with those of the gold standard SEM. Both techniques indicate that very high nozzle temperatures may lead to deformation of the filaments after deposition, although it may improve adhesion between layers

Figure 9 Bland-Altman plots comparing the OCT and SEM 3D measurements for height, spacing and width of the 3D samples printed with different temperatures

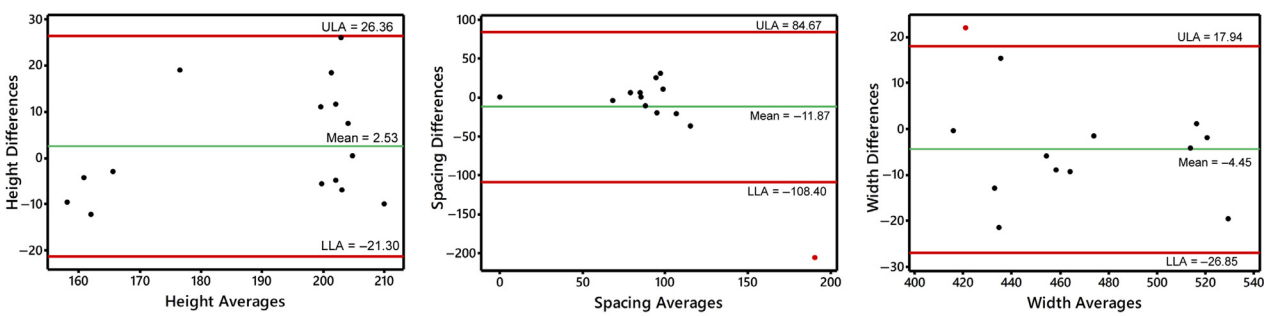

Notes: The green line represents the mean of the data points, while the red lines indicate the ULA and LLA for 95% confidence interval. Again, both techniques have high agreement on all measured features, with only one data point (width plot) falling outside the agreement region

molten material, analogous to what happens between adjacent roads), inducing an optical match between overlaid filaments. This phenomenon is not new to the OCT literature and is exploited by techniques of "index matching" or "optical clearing" to improve signal penetration (Brezinski *et al.*, 2001; Tuchin *et al.*, 2002). The evaluation of index matching in those samples is, therefore, related to the quality of layer adhesion in the FFF process. The adhesion (or bonding) between layers, just as the spacing between extruded roads, has also been shown, through SEM observations, to influence the mechanical properties of the printed sample (Wu *et al.*, 2018). Thus, through index matching, OCT images may, additionally, provide information on layer bonding. Nonetheless, further studies are required.

Inspection of FFF parts through OCT can, therefore, offer feedback for the effects of different printing temperatures, as well as provide information related to the sample's mechanical strength, and such visual inspection may help in finding the best printing setup. Nevertheless, Costa, Silva and Carneiro (Costa *et al.*, 2019) suggest that layer bonding and dimensional accuracy might have different optimal printing temperatures, which is in line with what we observed in our results. Therefore, the best printing settings should be adjusted taking into account the desired use of the part being fabricated.

Optical coherence tomography 3D reconstruction

Allied to the fact of being non-invasive and not requiring special sample preparation, OCT has the inherent ability to perform a 3D tomographic reconstruction of the sample, which is not viable through SEM. In that way, a new analysis may be possible, additional to the cross-sectional visualization, such as the identification of structures inside the 3D printed model.

To demonstrate this ability, the word "OCT" was included inside a sample by leaving out specific areas during the sample printing process, as illustrated by Figure 10(a). Figure 10(b) presents a 3D tomographic reconstruction of this sample (3D StudioMax®), based on OCT data collected. After reconstructing the 3D acquired data, it is possible to virtually slice it, creating different en-face visualizations and analyze the structures contained inside the sample. Moving the slice to the middle of our sample, it is possible to identify the word OCT that was printed. This depth-resolved en-face sectioning allows for better analysis of printing quality and defects inspection (and hidden structures, as shown here), and OCT provides a way to acquire it using a compact system, in a non-destructive manner.

Conclusions

In this work, we studied the performance of OCT to nondestructively evaluate FFF samples, using PLA filaments. The OCT technique was shown to be able to perform a cross-sectional analysis with a good correlation to the SEM gold standard when evaluating PLA.

OCT requires refractive index calibration for axial analysis, however, it was possible to measure the refractive index of the PLA (1.48 ± 0.04) using OCT itself, thus no additional technique is needed to perform dimensional analysis. After calibration, we demonstrate that quantitative dimensional analysis using OCT is in agreement with those obtained by SEM. The difference between measurements is of the order of the system resolution. In that way, we were able to non-destructively evaluate the printing quality with regard to spacing precision and, additionally, to discuss the effects of PLA heating on the final filament shape. Those analyses may offer valuable feedback for the printing process.

Figure 10 (a) The sample is designed with three layers. The first and the third layers consisted of longitudinal roads, while the middle one had a different structure, forming the word "OCT" through gaps in the mesh, as presented in an exploded view on the right side. (b) 3D reconstruction of the sample printed in PLA fused filaments. An inspection through different depths of the reconstruction enables the visualization of the "OCT" letters hidden within. The sample was placed over a piece of paper, which can be seen at the bottom of the reconstructed model

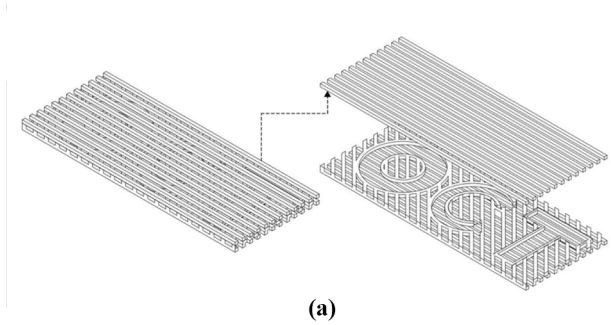

(a)

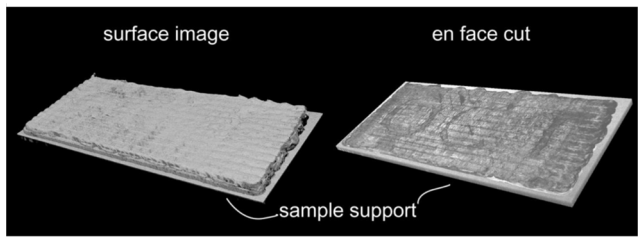

(b)

Furthermore, we also demonstrated that a full depth-resolved 3D reconstruction of the printed sample is possible only by using OCT. Such a model offers new analysis on the printing samples, such as *en-face* sectioning to evaluate internal structures. Future investigations could involve the use of OCT (including functional extensions such as polarization-sensitive OCT) on real-time applications, such as monitoring the printing process and offering inputs to a feedback loop control of FFF quality. Still, the use of OCT systems operating in wavelengths optimized for polymer analysis could provide higher penetration and better spatial resolution (Li *et al.*, 2017).

With the results presented in this paper, it is possible to state that OCT is a viable alternate technique to evaluate the quality of deposited layers on 3D printed components using the FFF technique and PLA filaments.

References

Berman, B. (2012), "3-D printing: the new industrial revolution", *Business Horizons*, Vol. 55 No. 2.

Brezinski, M., Saunders, K., Jesser, C., Li, X. and Fujimoto, J. (2001), "Index matching to improve optical coherence tomography imaging through blood", *Circulation*, Vol. 103 No. 15.

Costa, A.E., Ferreira da Silva, A. and Sousa Carneiro, O. (2019), "A study on extruded filament bonding in fused filament fabrication", *Rapid Prototyping Journal*, Vol. 25 No. 3, pp. 555-565.

Cuan-Urquizo, E., Barocio, E., Tejada-Ortigoza, V., Pipes, R. B., Rodriguez, C.A. and Roman-Flores, A. (2019), "Characterization of the mechanical properties of FFF structures and materials: a review on the experimental, computational and theoretical approaches", *Materials*, Vol. 12 No. 6, p. 895.

Davis, C.S., Hillgartner, K.E., Han, S.H. and Seppala, J.E. (2017), "Mechanical strength of welding zones produced by polymer extrusion additive manufacturing", *Additive Manufacturing*, Vol. 16, pp. 162-166.

De Freitas, A.Z., Amaral, M.M. and Raele, M.P. (2010), "'Optical coherence tomography: development and applications", in Duarte F.J. (Ed.), *Laser Pulse Phenomena and Applications*, IntechOpen, pp. 409-432, doi: 10.5772/12899.

DePond, P.J., Guss, G., Ly, S., Calta, N.P., Deane, D., Khairallah, S. and Matthews, M.J. (2018), "In situ measurements of layer roughness during laser powder bed fusion additive manufacturing using low coherence scanning interferometry", *Materials and Design*, doi: 10.1016/j.matdes.2018.05.050.

Gardner, M.R., Lewis, A., Park, J., McElroy, A.B., Estrada, A.D., Fish, S., Beaman, J.J., Jr,. and Milner, T.E. (2018), "In situ process monitoring in selective laser sintering using optical coherence tomography", *Optical Engineering*, Vol. 57 No. 4, pp. 1-5.

Gebisa, A.W. and Lemu, H.G. (2018), "Investigating effects of fused-deposition modeling (FDM) processing parameters on flexural properties of ULTEM 9085 using designed experiment", *Materials*, Vol. 11 No. 4, p. 500.

Goncalves, C.M.B., Coutinho, J.A.P., Marrucho, I.M., *et al.* (2010), "Optical properties", in Auras, R.A. (Ed.), *Poly (Lactic Acid): Synthesis, Structures, Properties, Processing, and Applications*, 1 st ed., WILEY, pp. 97-112.

Guan, G., Hirsch, M., Lu, Z.H., Childs, D.T., Matcher, S.J., Goodridge, R., Groom, K.M. and Clare, A.T. (2015), "Evaluation of selective laser sintering processes by optical coherence tomography", *Materials and Design*, doi: 10.1016/j.matdes.2015.09.084.

Guo, N. and Leu, M.C. (2013), "Additive manufacturing: technology, applications and research needs", *Frontiers of Mechanical Engineering*, Vol. 8 No. 3.

Hirsch, M., Patel, R., Li, W., Guan, G., Leach, R.K., Sharples, S.D. and Clare, A.T. (2017), "Assessing the capability of in-situ nondestructive analysis during layer based additive manufacture", *Additive Manufacturing*, Vol. 13.

Hollister, S.J., Flanagan, C.L., Zopf, D.A., Morrison, R.J., Nasser, H., Patel, J.J., Ebramzadeh, E., Sangiorgio, S.N., Wheeler, M.B. and Green, G.E. (2015), "Design control for clinical translation of 3D printed modular scaffolds", *Annals of Biomedical Engineering*, Vol. 43 No. 3, pp. 774-786.

Huang, D., Swanson, E.A., Lin, C.P., Schuman, J.S., Stinson, W.G., Chang, W., Hee, M.R., Flotte, T., Gregory, K. and Puliafito, C.A. (1991), "Optical coherence tomography", *Science*, Vol. 254 No. 5035, pp. 1178-1181.

Kim, H., Lin, Y. and Tseng, T.-L.B. (2018), "A review on quality control in additive manufacturing", *Rapid Prototyping Journal*, Vol. 24 No. 3, pp. 645-669.

Kuznetsov, V.E., Solonin, A.N., Urzhumtsev, O.D., Schilling, R. and Tavitov, A.G. (2018), "Strength of PLA components fabricated with fused deposition technology using a desktop 3D printer as a function of geometrical parameters of the process", *Polymers*, Vol. 10 No. 3, p. 313.

Lanzotti, A., Grasso, M., Staiano, G. and Martorelli, M. (2015), "The impact of process parameters on mechanical properties of parts fabricated in PLA with an open-source 3-D printer", *Rapid Prototyping Journal*, Vol. 21 No. 5, pp. 604-617.

Li, Y., Jing, J., Heidari, E., Zhu, J., Qu, Y. and Chen, Z. (2017), "Intravascular optical coherence tomography for characterization of atherosclerosis with a 1.7 micron swept-source laser", *Scientific Reports*, Vol. 7 No. 1.

McIlroy, C. and Olmsted, P.D. (2017), "Disentanglement effects on welding behaviour of polymer melts during the fused-filament-fabrication method for additive manufacturing", *Polymer*, Vol. 123.

Mohamed, O.A., Masood, S.H., Bhowmik, J.L., Nikzad, M. and Azadmanjiri, J. (2016), "Effect of process parameters on dynamic mechanical performance of FDM PC/ABS printed parts through design of experiment", *Journal of Materials Engineering and Performance*, Vol. 25 No. 7, pp. 2922-2935.

Rengier, F., Mehndiratta, A., Von Tengg-Kobligk, H., Zechmann, C.M., Unterhinninghofen, R., Kauczor, H.U. and Giesel, F.L. (2010), "3D printing based on imaging data: review of medical applications", *International Journal of Computer Assisted Radiology and Surgery*, Vol. 5 No. 4.

Song, Y., Li, Y., Song, W., Yee, K., Lee, K.Y. and Tagarielli, V.L. (2017), "Measurements of the mechanical response of unidirectional 3D-printed PLA", *Materials and Design*, doi: 10.1016/j.matdes.2017.03.051.

Torrado Perez, A.R., Roberson, D.A. and Wicker, R.B. (2014), "Fracture surface analysis of 3D-printed tensile specimens of novel ABS-based materials", *Journal of Failure Analysis and Prevention*, Vol. 14 No. 3.

Tuchin, V.V., Xu, X. and Wang, R.K. (2002), "Dynamic optical coherence tomography in studies of optical clearing, sedimentation, and aggregation of immersed blood", *Applied Optics*, Vol. 41 No. 1, pp. 258-271.

Tymrak, B.M., Kreiger, M. and Pearce, J.M. (2014), "Mechanical properties of components fabricated with open-source 3-D printers under realistic environmental conditions", *Materials and Design*, doi: 10.1016/j.matdes.2014.02.038.

Wu, W., Ye, W., Geng, P., Wang, Y., Li, G., Hu, X. and Zhao, J. (2018), "3D printing of thermoplastic PI and interlayer bonding evaluation", *Materials Letters*, Vol. 229, pp. 206-209.

Corresponding author

Marcus Paulo Raele can be contacted at: mpraele@ipen.br